Available online at www.sciencedirect.com
SCIENCE DIRECT
Tectonophysics 414 (2006) 97–116
TECTONOPHYSICS
www.elsevier.com/locate/tecto

Experimental and texture-derived P-wave anisotropy of principal rocks from the TRANSALP traverse: An aid for the interpretation of seismic field data

Klaus Ullemeyer [a,*], Siegfried Siegesmund [b], Patrick N.J. Rasolofosaon [c], Jan H. Behrmann [a]

[a] *Geologisches Institut, Universität Freiburg, Albertstraße 23-B, D-79104 Freiburg, Germany*
[b] *Geowissenschaftliches Zentrum der Universität Göttingen (GZG), Goldschmidtstraße 3, D-37077 Göttingen, Germany*
[c] *Institut Français du Pétrole (IFP), Geophysics Department, 1 et 4 avenue de Bois Préau, F-92852 Rueil Malmaison Cedex, France*

Received 1 September 2004; received in revised form 30 June 2005; accepted 4 October 2005
Available online 10 January 2006

Abstract

A representative suite of deformed, metamorphic rocks from the TRANSALP reflection seismic traverse in the Eastern Alps was studied in the laboratory with respect to elastic properties and whole-rock texture. Compressional wave (P-wave) velocities and their anisotropies were measured at various experimental conditions (dry, wet, confining pressure), and compared to the texture-related component of anisotropy. Here 'texture' refers to crystallographic preferred orientations (CPOs), which were determined by neutron texture goniometry. In gneisses and schists P-wave anisotropies are mainly controlled by the microcrack fabric. In marbles and amphibolites CPO contributes very significantly to anisotropy. At 200 MPa confining pressure the degree of anisotropy is between 5% and 15%, depending on rock composition and/or CPO intensity. Special emphasis was also put on discussing possible effects of fluids on seismic velocity and anisotropy. Distributions of water-filled microcracks and pores are distinctly anisotropic, with maximum contribution to bulk rock velocity mostly parallel to the foliation pole. Decreasing P-wave velocity and increasing anisotropy of immersed samples may be explained by crack-induced changes of the elastic moduli of bulk rock. The main conclusion regarding interpretation of TRANSALP data is that strong reflections in the deep Alpine crust are probably due to marble–gneiss and metabasite–gneiss contacts, although P-wave anisotropy and boundaries between zones of 'dry' or 'wet' series may contribute to reflectivity to some extent.

Keywords: Elastic rock properties; Anisotropy of compressional wave velocities; Texture (crystallographic preferred orientation); Seismic reflectivity of the crust; Crack fabric; Porosity; Fluids

1. Introduction

Correct interpretations of seismic field measurements are crucially dependent on the understanding of the elastic rock properties. Especially the compressional wave (P-wave, V_p) velocities measured in the laboratory or calculated from crystallographic preferred orientations (CPOs, in the following referred to as textures)

* Corresponding author. Tel.: +49 761 203 7605; fax: +49 761 203 6496.
E-mail address: klaus.ullemeyer@geologie.uni-freiburg.de (K. Ullemeyer).

0040-1951/$ - see front matter © 2005 Elsevier B.V. All rights reserved.
doi:10.1016/j.tecto.2005.10.024

can be a helpful tool (see, e.g., reviews by Siegesmund, 1996; Mainprice et al., 2000). In the general case elastic behaviour of rock is anisotropic, with the degree of anisotropy mainly depending on the textures of the principal rock-forming minerals, the elastic constants of the minerals, the microscopic and macroscopic crack fabric (often referred to as 'porosity' in geophysical studies), the rock modal composition, and the *P–T* conditions (e.g., Kern, 1993). Also, compositional layering may have significant influence, whereas grain shape preferred orientations are believed to play a minor role in creating elastic anisotropy. The effect of the crack fabric—including the possible influence of enclosed fluids—is termed 'extrinsic' component of elastic anisotropy, whereas all the other factors mentioned above form the 'intrinsic' component of elastic anisotropy (Kern, 1993). Numerous experiments confirmed that the influence of the crack fabric decreases with burial depth following progressive crack closure under increasing lithostatic load (e.g., Christensen, 1965; Kern et al., 2002; Pros et al., 2003). Therefore, the effect of the mineral textures is assumed to dominate deep in the Earth's crust. This holds especially true for rocks containing significant amounts of highly anisotropic minerals like, e.g., phyllosilicate minerals (Barruol et al., 1992; Godfrey et al., 2000) or hornblende (Siegesmund, 1996). Whether all cracks are actually closed at greater crustal depths is discussed controversially (e.g., Mooney and Meissner, 1992; Lüschen et al., 1996; Rabbel et al., 1998), so that quantitative knowledge of the texture-induced component of elastic anisotropy may guide evaluation of seismic measurements as to identify zones of open, fluid-filled cracks and associated high permeability deep in the crust.

In this study we make reference to the recently completed TRANSALP crustal-scale reflection seismic project (TRANSALP Working group, 2002) in the Eastern Alps. We have sampled representative rocks from the large-scale tectonic units in the crystalline basement of the Eastern Alps along the central section of the 300 km long TRANSALP traverse located roughly between the cities of Munich and Treviso (N of Venice; Fig. 1A, B). Our aim is to document the results of quantitative texture analyses by neutron diffraction, and compressional wave velocity measurements on the rocks sampled. P-wave velocity measurements on common rocks close to the TRANSALP traverse were already carried out by Mazzoli et al. (2002) for a limited number of sample directions leading to restricted information on elastic anisotropy. We measured P-wave velocities in many sample directions to obtain the complete information on P-wave anisotropy, and varied experimental conditions to gain anisotropy information for different sample states. Concluding, we will discuss the contributions of texture and microfabrics to seismic anisotropy, and attempt to assess its importance in the interpretation of the TRANSALP reflection seismic data.

The Eastern Alps are part of a collisional orogen arising from the convergence of the Eurasian and Adriatic plates. Movements started in the Cretaceous, and continued through the Tertiary along a complex convergent path (Platt et al., 1989). This involved large increments of WNW to NW-directed displacement of the upper, Austroalpine over the lower, Pennine units (Fig. 1A, B) and associated dextrally and sinistrally transpressive deformations (e.g., Behrmann, 1990; Behrmann and Frisch, 1990). One of the consequences of such transpressive ductile overprint is large E−W stretching and generation of strong and large-scale textural and fabric anisotropy within the Pennine basement units (e.g., Lammerer, 1986; Behrmann, 1990; Lammerer and Weger, 1998) and in the Austroalpine to the south of the Tauern Window (e.g., Mancktelow et al., 2001). In the seismic section, the bivergent structure of the Eastern Alps is evident, with the southward dipping 'Sub Tauern Ramp' and the northward dipping 'Sub Dolomites Ramp' as the most prominent thrust planes (TRANSALP Working group, 2002; Fig. 1C indicates location of the 'Sub Tauern Ramp' and the seismic structure of the upper crust in the section of interest in relation to a tentative geological cross-section). Cross-line observations from the central part of the TRANSALP seismic profile clearly indicate anisotropy of P-wave propagation velocities higher than 10% on a regional scale with the higher velocities directed E−W in agreement with the above mentioned overall stretching direction in the basement units (Millahn et al., 2005—this volume).

In order to gain information on the sources of anisotropy on the laboratory scale, P-wave velocity measurements were performed on 12 samples from the main lithological units of the Tauern Window and neighbouring series, going along with corresponding calculation of P-wave anisotropy from the mineral textures, the modal composition of rock, and the single crystal elastic constants. Since all the measurements should be representative for large rock bodies, the samples were carefully selected with respect to this demand: sample composition corresponds to the average composition of particular lithotypes, moreover, inhomogeneities at sample scale like, e.g., compositional layering were avoided to ensure representative measurements. Spherical samples were used for the measurements to achieve the complete 3D information

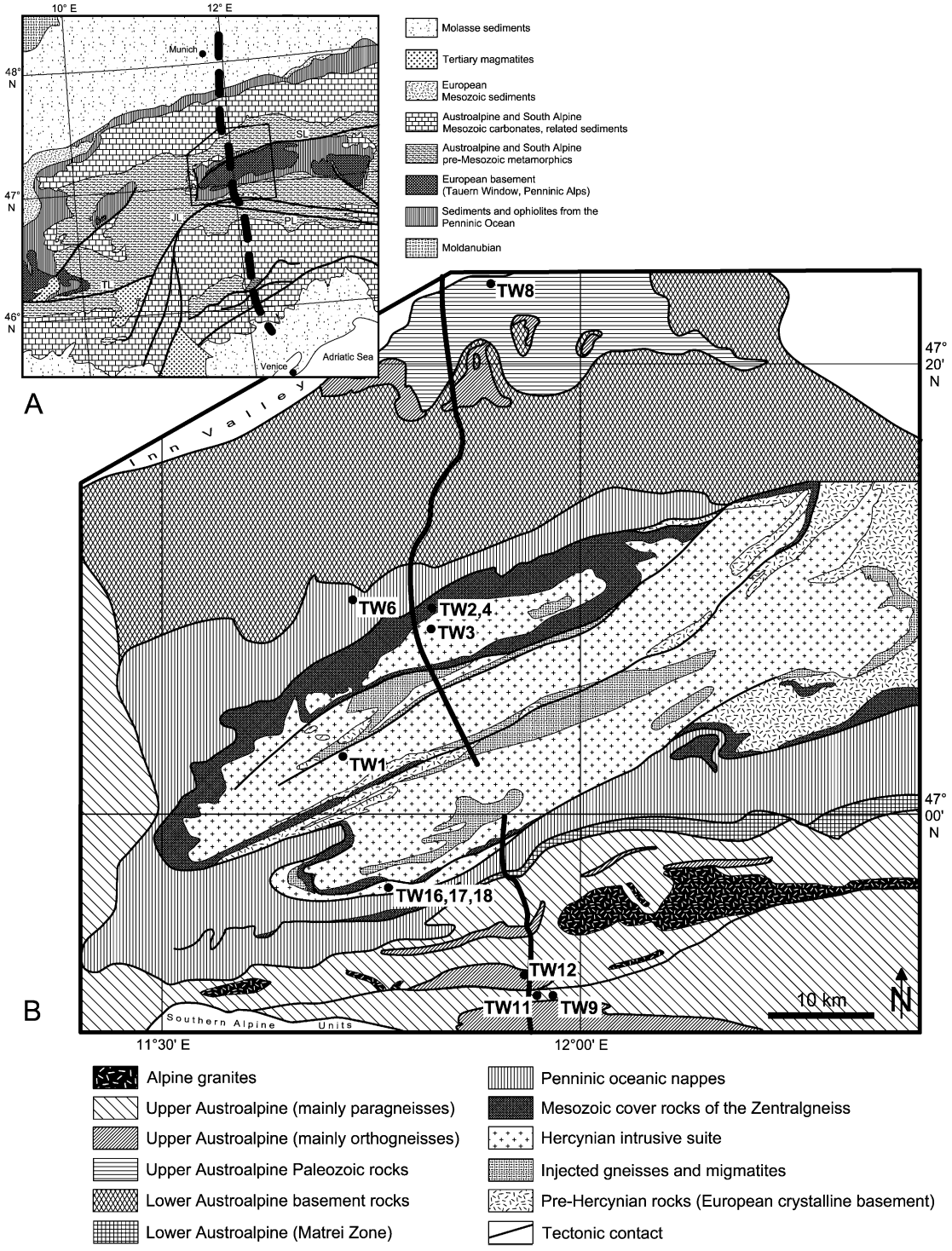

Fig. 1. (A) Geological sketch map of the central segment of the Eastern Alps, showing location of the TRANSALP traverse and the major tectonic units. (B) Location map along the central part of the TRANSALP traverse (modified after TRANSALP Working group, 2002). (C) Geological profile along the central part of the seismic section (modified after Lammerer, pers. communication). Sample locations are indicated in (B) and (C).

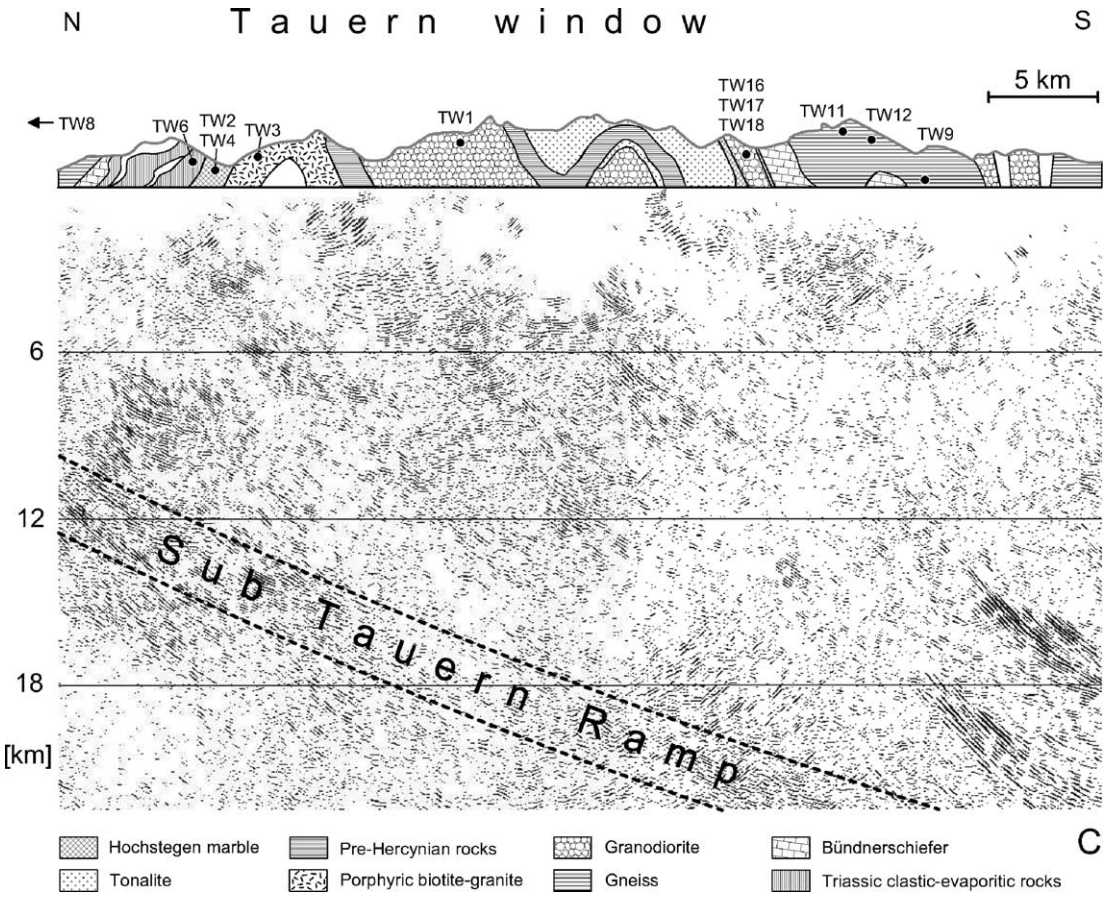

Fig. 1. (*continued*).

on P-wave anisotropy. Experimental settings include measurements at a confining pressure of P_{conf}=200 MPa, as well as measurements on dry and water-saturated samples at atmospheric pressure. In addition, the progressive closure of microcracks was documented by P-wave velocity measurements up to P_{conf}=400 MPa for the three principal directions of the structural reference frame, which is determined by foliation and lineation, respectively. A detailed description of the applied experimental techniques is given in the section below. From variation of the experimental conditions and from the comparison of experimental and calculated (texture-derived) velocity distribution information on the degree of anisotropy and the relative influence of the mineral textures and the crack fabric on anisotropy is expected.

In the discussion of our results, there is effort on the effect of fluids on the reflectivity of the seismic crust. Mineral reactions, mass transfer in shear zones etc. indicate that fluid-filled pore space should be present in the continental crust. Decrease of the elastic wave velocities in dependence on the amount of fluids and the effective pore pressure, and therefore variation of the elastic moduli and Poisson's ratio must be expected (Nur and Simmons, 1969). In fact, fluids were observed in the crystalline basement rocks of the ultra-deep KTB exploration borehole (Kontny et al., 1994), an effect predicted by the interpretation of seismic data (Lüschen et al., 1993). In contrast, fluids seem to be an unlike explanation for shear wave anisotropies observed at Urach, SW Germany (Rabbel et al., 1998). Here we aim to characterize the effect of fluids on P-wave velocity and velocity anisotropy quantitatively on the laboratory scale. The pore space distribution observed at surface conditions is used as a first-order image of pore space distribution in the crust, and in our calculations its volume fractions are varied to model P-wave velocity and anisotropy variations.

In order to get the connection to TRANSALP seismic profiling, reflection coefficients are calculated for simple lithological interfaces and their variability in dependence on rock composition and rock state (dry–wet) is discussed.

2. Methods

2.1. Texture measurements and calculation of P-wave velocity distributions from the textures

Texture measurements follow the goal to calculate bulk V_p distributions from the mineral textures, the mineral elastic constants and the modal composition of rock. The calculated P-wave distributions represent an upper limit of P-wave velocities, as all the other controlling parameters of rock elasticity lead to velocity decrease. The texture measurements were performed at the neutron time-of-flight texture diffractometer SKAT at the Frank Laboratory of Neutron Physics at JINR, Dubna, Russia (Ullemeyer et al., 1998). We made use of the main advantage of neutrons that large sample volumes can be investigated due to low absorption of neutrons in matter. Integration over large sample volumes better resembles the bulk texture, an important feature especially for the calculation of global physical rock properties. The large beam cross-section of 85×50 mm^2 at Dubna allows investigation of the same spherical samples used for the P-wave measurements, with the obvious advantage that sample-induced errors can be minimized. Moreover, the good spectral resolution of the instrument ($\Delta d/d \approx 0.5\%$ at $d=2$ Å) minimizes peak overlapping in the time-of-flight patterns and allows extraction of a sufficient number of experimental pole figures for subsequent quantitative texture analysis. Texture analyses were carried out for the main rock constituents applying the WIMV algorithm (Matthies and Vinel, 1982). Including the elastic tensors of particular minerals and their volume fractions, the P-wave velocity distributions of bulk rock were averaged from the mineral textures. In case of missing texture, mean values of the single crystal elastic constants were used. Several averaging techniques are described in the literature (see Tomé, 1998, for an overview). We applied the Voigt approximation, which assumes homogeneous strain distribution within the sample and therefore gives an upper limit for elastic deformation and consequently the uppermost possible P-wave velocity at all. This property of the Voigt method should be kept in mind when judging the calculated P-wave velocity distributions. Both the WIMV algorithm and the Voigt approximation are included in the BEARTEX software package (Wenk et al., 1998).

2.2. P-wave velocity measurements

P-wave velocity measurements applying the pulse transmission technique (Birch, 1960) were carried out at various experimental conditions to gain information on as many controlling parameters of P-wave anisotropy as possible. Polished spherical samples with a diameter of (50 ± 0.02) mm were prepared, the ultrasonic measurements were performed in 100 sample directions on the surface of the spheres to obtain complete V_p distributions. The samples were mounted in a two axes positioning system, allowing repeated rotation of the sample around its vertical axis and simultaneous inclination of both transmitter and receiver, which are located at opposite sides of the sphere (Pros et al., 1998). The natural frequency of applied piezoceramic transducers was 2 MHz.

(i) for P-wave velocity measurements at confining pressure $P_{conf}=200$ MPa corresponding to a crustal depth of approx. 6 km, the whole equipment was placed in a pressure vessel filled with hydraulic oil (Pros et al., 1998). The samples were protected by an epoxy resin film, its effect on the travel times of the ultrasonic signal was taken into consideration during subsequent calculations. At 200 MPa formerly open cracks and open pore space are mostly closed and their influence on the elastic rock properties is small or even can be neglected (Kern et al., 2002). Since all the remaining factors influencing P-wave anisotropy except the mineral textures are minor, the resulting P-wave distributions should approximate the texture-derived ones.

(ii) in order to characterize the closure of cracks with increasing confining pressure, P-wave velocity measurements within the pressure range 2~400 MPa ($P_{conf}=2$–20–50–100–200–400 MPa) were performed on cylindrical samples for the three principal directions of the structural reference frame. The three series were combined and the model function proposed by Pros et al. (1998),

$$V_p = a_p + b_p P_{conf} - c_p 10^{-P_{conf}/d_p}, \quad (1)$$

was fit to the data, assuming that the 'intrinsic' contribution to the velocity–pressure equation may be described by a linear trend and the 'extrinsic' (crack-related) contribution by an exponential law (Pros et al., 1998). Parameters obtained from the fitting procedure are the 'intrinsic' reference velocity $a_P=V_{P_0}$ of a crack-free sample at zero pressure, the 'intrinsic' pressure derivative $b_P=dV_p/dP$ of the crack-free sample, the crack influence $c_P=V_{P_c}$ at zero pressure, and the confining pressure $d_P=P_{0.1}$, at which the influence of cracks is reduced to 10% (Fig. 2 illustrates the coefficients of applied model function). Reliability of the above proposed decomposition of the velocity–pressure equation into two components has not yet been proven, hence, all functional parameters, and consequently the crack-induced velocity decrease $\Delta V_p = -c_p 10^{-P_{conf}/d_p}$

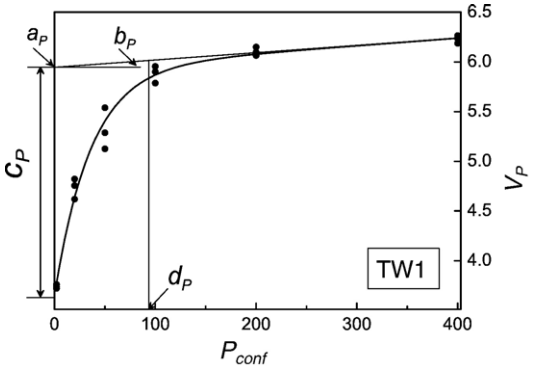

Fig. 2. Coefficients of applied model function and their physical meaning (Pros et al., 1998). $a_P=V_{P_0}$: 'intrinsic' velocity at zero pressure; $b_P=dV_P/dP$: 'intrinsic' pressure derivative; $c_P=V_{P_0}$: crack influence at zero pressure; $d_P=P_{0.1}$: confining pressure, at which the remaining influence of cracks is 10%.

at P_{conf}=200 MPa we are mainly interested in, may be affected by a large error level. This should be kept in mind when judging velocity differences ΔV_P. The measurements were performed at GZG, Göttingen.

(iii) 3D P-wave distributions were measured also on oven-dried and water-immersed samples at atmospheric pressure and room temperature at IFP, Rueil–Malmaison. For a first experimental run, the samples were dried at 50 °C for three days, assuming, that the pore volume was now completely filled with air. P-wave distributions were measured in 100 sample directions as described above. Subsequently, the air was replaced (partly, perhaps completely) by water in a low pressure chamber, and the P-wave measurements were repeated. Compressional wave velocities in air and water are different (0.34 and 1.53 km s^{-1}, respectively), hence, bulk rock velocity increases in the immersed sample. Since the P-wave velocities in air and water are isotropic, any anisotropy observed in the difference velocity distribution,

$$\Delta V_p(\alpha,\beta) = V_p(\text{wet})(\alpha,\beta) - V_p(\text{dry})(\alpha,\beta), \qquad (2)$$

where angles (α,β) indicate particular sample direction in polar coordinates, must be due to an anisotropic distribution of pore space. For the description of pore space anisotropy, the replacement of air by water is allowed to be incomplete, because all the unchanged contributions to bulk rock velocity — in particular, the contributions of the rock matrix and still air-filled pore fraction — vanish while calculating the differential velocity matrix. In fact, the degree of saturation cannot be determined. Porosity measurements by buoyancy weighting therefore record the water-filled fraction of pores only (see Table 2 for the results), and particular velocity contributions of water-filled and air-filled pores are unknown. Actually measured velocity magnitudes, therefore, should not be interpreted. For the description of pore space anisotropy, velocity difference matrices are normalized such that $\Delta V_{P_{mean}} = 1$, i.e., the stereoplots directly reflect spatial distributions of anisotropy coefficients A (α,β). The theoretical background of the method can be found in Arts et al. (1996). Although the technique was developed to evaluate microcrack geometry from 3D P-wave measurements obtained at various confining pressures, the principle is also applicable for our purposes.

3. Sample description

Fabric elements effecting the elastic rock properties are the mineralogical composition, apparent foliations and compositional layering, the pore volume, grain shape and grain size inhomogeneities, whereas grain internal structures are assumed to have minor influence on the elastic anisotropy of minerals. Modal composition was determined by means of Rietveld refinement method on X-ray powder diffraction data using commercially available software (Bergmann et al., 1998; see Table 1 for the results). The software considers textural effects with transverse isotropic symmetry, thus, the influence of phyllosilicate basal plane preferred orientations (resulting from powder sample preparation) on the results of refinement could be minimized and the results of quantitative phase analyses are, therefore, expected to be reliable. The overall matrix density can be simply calculated from the weight and the volume of the samples (Table 2).

For a generalized description, the samples are comprised into four groups: marbles, amphibolites, gneisses and schists. In a section parallel to the predominant lineation (which may be a stretching lineation or the axis of microfolds) and perpendicular to the main foliation, the grain fabrics can be characterized as follows.

Both the marble samples (TW2, TW4) are mainly composed of calcite (>90%), minor quartz, dolomite and muscovite may occur (see Table 1). Particular mineral phases are homogeneously distributed, no compositional layering can be observed. The average grain size of sample TW2 is approx. 200 μm, a weak foliation plane is defined by slightly elongated grains parallel to the macroscopic lineation (Fig. 3A). The grain fabric of sample TW4 is similar, however, mean grain size is smaller (approx. 50 μm) and no foliation plane can be recognized due to missing grain shape anisotropy. Pore volumes are the smallest of all samples (TW2: 0.55%,

Table 1
Results of X-ray quantitative phase analyses applying Rietveld refinement method

Rock type		Composition [vol.%]								
		Qtz	Plg	Pfs	Mus	Bt	Cc	Dol	Chl	Hbl
TW1	Augen gneiss	***32***	***32***	***23***	12	1				
TW2	Marble	3			***4***		***92***	1		
TW3	Bt augen gneiss	***23***	***26***	16	22	7	2		4	
TW4	Marble	2					***98***			
TW6	Slate	***35***	***36***		25		3			
TW8	Slate	***35***	***25***	2	28		1		8	
TW9	Fine-grained gneiss	***38***	25	3	***19***	***7***			***8***	
TW11	Amphibolite	2		6		6			4	***82***
TW12	Gneiss	***32***	***33***	17	17					
TW16	Mylonitic gneiss	***31***	***25***	13	29		2			
TW17[a]	Medium-grained gneiss	***40***	***45***	5	10					
TW18	Gneiss	***37***	***48***	5	8		2			

Bold italic numbers indicate preferred orientation of particular minerals.
Qtz: quartz, Plg: plagioclase, Pfs: potassic feldspar, Mus: muscovite, Bt: biotite, Cc: calcite, Dol: dolomite, Chl: chlorite, Hbl: hornblende.
[a] The composition of sample TW17 was estimated in thin section.

TW4: 0.29%), whereas matrix densities are almost identical (ρ=2740 and 2730 kg m^{-3}, respectively; Table 2).

Although amphibolites are scarce along the TRANSALP traverse, a single sample (TW11) was collected. A matrix density of ρ=3150 kg m^{-3} was estimated, which is about 15% higher than the average matrix density of the gneisses (Table 2). The sample mainly consists of hornblende (82%) and minor quartz, potassic feldspar, biotite and chlorite (Table 1). The hornblende grain size spectrum ranges from 100 to 1000 μm. Elongated recrystallized grains, which can be derived from older host grains, define a local foliation (arrows in Fig. 3B). The grain size of the other mineral phases is much smaller (50~100 μm), the grain shape is isotropic. The pore volume is 0.81% (Table 2).

The gneisses (TW1, TW3, TW9, TW12, TW16, TW17, TW18) are variable with respect to composition, meso- and microfabric. All the samples contain quartz, feldspars and muscovite in various amounts (quartz: 23~40%, plagioclase: 25~48%, potassic feldspar: 3~23%, muscovite: 8~29%). The volume fractions of the other minerals, like biotite, chlorite and calcite are much smaller than 10% (refer to Table 1). Grain sizes vary within a broad interval. Porphyroclasts in augen gneisses are approximately 0.5 cm in size, whereas recrystallized grains display a minimal grain size of

Table 2
General sample characteristics: porosity and matrix density ρ, as well as the 'intrinsic' reference velocity V_{P_0} at zero pressure, the 'intrinsic' pressure derivative dV_P/dP, the crack influence V_{P_c} at zero pressure, the confining pressure $P_{0.1}$, at which the remaining influence of cracks is 10%, and the crack influence ΔV_P at P_{conf}=200 MPa

	Porosity [vol.%]	ρ [kg m^{-3}]	V_{P_0} [km s^{-1}]	dV_P/dP [10^{-3} km s^{-1} MPa^{-1}]	V_{P_c} [km s^{-1}]	$P_{0.1}$ [MPa]	ΔV_P [km s^{-1}]
TW1	1.47	2640	5.95	0.73	2.28	85	−0.010
TW2	0.55	2740	6.37	0.27	0.56	45	0.000
TW3	0.89	2720	5.93	0.63	1.85	100	−0.019
TW4	0.29	2730	6.34	0.69	0.47	64	0.000
TW6	0.73	2710	6.04	0.33	2.08	99	−0.020
TW8	1.72	2740	5.94	0.53	1.94	83	−0.007
TW9	0.90	2800	5.86	1.02	1.45	103	−0.017
TW11	0.81	3150	6.29	1.46	1.82	68	−0.002
TW12	1.30	2660	5.74	1.48	2.04	60	−0.001
TW16	1.26	2680	5.62	1.31	2.18	91	−0.013
TW17	3.05	2700	5.52	1.36	2.05	109	−0.030
TW18	0.99	2680	5.83	1.27	3.13	48	0.000

Note that the porosity represents the immersed portion of bulk rock porosity only. For discussion refer to the text.

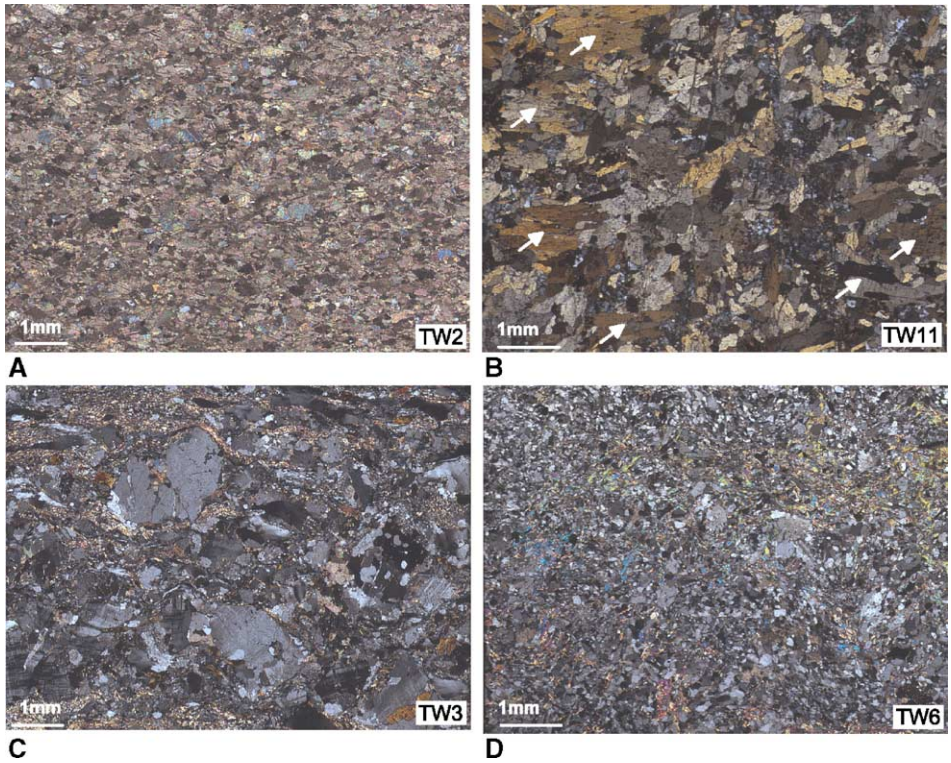

Fig. 3. Typical microstructures, illustrated by four samples in sections perpendicular to the macroscopic foliation and parallel to the lineation. (A) Homogeneous and fine-grained fabric of the marbles. (B) Amphibolite, characterized by large hornblende parent grains (arrows) and recrystallized grains with smaller grain size. Fine-grained feldspars and phyllosilicates are evenly distributed. (C) Typical gneiss microfabric with coarse-grained clasts and fine-grained phyllosilicates arranged on irregular cleavage planes. (D) Fine-grained slate, folded in the mm to cm scale.

30 μm (Fig. 3C). Although the volume of 65 cm^3 of the studied samples is rather large, inhomogeneities in mineral distribution, caused by the porphyroclasts need to be considered. This is a crucial factor for the P-wave measurements, whereas the influence of porphyroclasts on the scattered intensities in the neutron texture experiment can be handled much easier. The pore volume of the gneisses ranges from 0.89% to 3.05%, matrix density varies between 2640 and 2800 kg m^{-3}.

The schists (samples TW6, TW8) are mainly composed of quartz (35%), plagioclase (25~36%) and muscovite (25~28%). Chlorite may occur in considerable amounts, whereas calcite and potassic feldspar are scarce (Table 1). Both samples are fine-grained, the grain size range is 30~300 μm, with the average grain size close to the lower boundary of the interval. The mineral distribution is homogeneous, no compositional layering can be observed. Microfolds are not apparent in hand specimen, but can be observed in thin section (Fig. 3D). The estimated matrix densities of the samples are 2710 kg m^{-3} (TW6) and 2740 kg m^{-3} (TW8), the pore volumes are 0.73% and 1.72%, respectively.

4. Data

4.1. Textures and calculated P-wave velocity distributions

The degree of lattice preferred orientation was quantified with the texture index J, which has a lower limit of 1.0 in case of missing preferred orientation (Bunge, 1982). In Fig. 4, the texture indices of all the mineral phases displaying preferred orientation are given, Fig. 5 shows significant pole figures of few samples with typical textures. Although quantitative texture analyses were tried for all rock constituents, pronounced preferred orientations are valid only for more or less monophase samples and for certain minerals in polyphase samples. Occasionally, the textures are very weak (e.g. samples TW6, TW17, TW18). Quartz generally shows crystallographic preferred orientations, except in cases of small volume fractions (samples TW2, TW4, TW11). The degree of preferred orientation is typically $J<1.3$. This value is smaller than for plagioclase ($J<1.5$), which mostly shows clear but weak

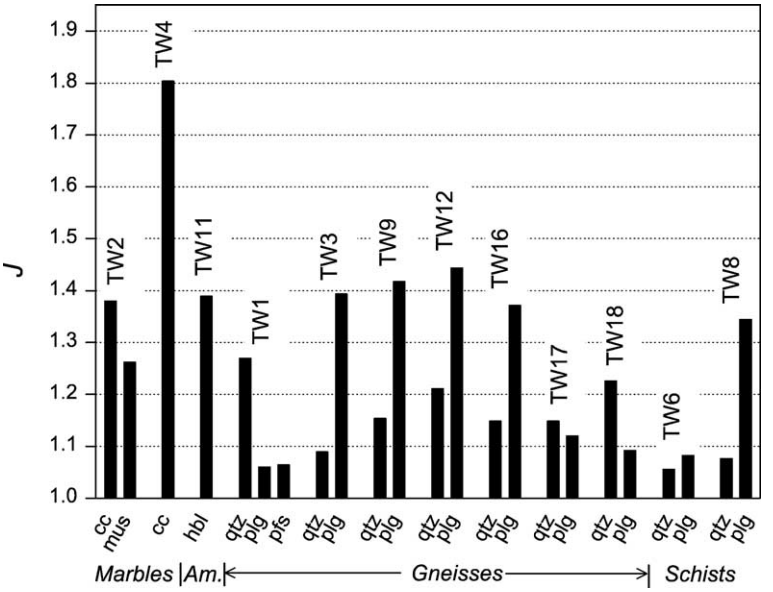

Fig. 4. Texture index J (=degree of lattice preferred orientation) of the texturized mineral phases. $J=1$ corresponds to a random distribution (Bunge, 1982). *Am.*: amphibolite.

preferred orientation. Muscovite, biotite and chlorite are randomly oriented, except for samples TW2 and TW9. This is surprising, since pronounced P-wave anisotropies of phyllonites reported by Mazzoli et al. (2002) let us assume well-developed phyllosilicate CPOs. Phyllosilicate minerals are indicators for foliations due to their grain shape related reorientation mechanism. Consequently, missing preferred orientation indicates absence of a predominant foliation at sample scale. For the schists (samples TW6, TW8), this observation can be confirmed in thin section, where the random orientation of the phyllosilicates can be easily inferred (see micrograph of sample TW6 in Fig. 3D). The gneisses are either folded in the micro- to mesoscale or display inhomogeneous grain size distributions with large clasts and inhomogeneous flow around the clasts (augen gneiss), both leading to the observed random orientation of the phyllosilicates. Preferred orientation of potassic feldspar could be detected only in sample TW1, the degree of preferred orientation is very small ($J=1.06$). The hornblende texture in sample TW11 is well-pronounced ($J=1.39$), although the grain shape preferred orientation of hornblende appears to be random in thin section (Fig. 3B).

Calculation of bulk rock P-wave velocity distributions from the mineral textures applying Voigt boundary condition was based on mineral elastic constants from literature. Fig. 6 gives particular P-wave distributions, anisotropies $(V_{P_{max}}-V_{P_{min}})/V_{P_{mean}}$ ($V_{P_{max}}$, $V_{P_{min}}$ and $V_{P_{mean}}$ refer to the maximum, minimum and mean P-wave velocities), and references. All the texture-derived P-wave velocity distributions and anisotropy parameters are compiled in Figs. 7 and 8.

Most of the gneisses show a very weak texture-derived P-wave velocity anisotropy A_{tex} ranging from 0.9~1.7%, except sample TW9 with $A_{tex}=3.2\%$ (Fig. 8). Weak or missing textures may explain this observation. Sample TW9 represents the only sample showing preferred orientation of the phyllosilicates (refer to Fig. 5 for the summarized muscovite+biotite+chlorite basal plane pole figure). In agreement with a phyllosilicate volume fraction of 34%, velocity anisotropy may be assigned to the phyllosilicates (but refer to discussion in Section 5.). Highest velocity anisotropy is due to the marbles (samples TW2 and TW4; $A_{tex}=7.2\%$ and 9.6%, respectively). The almost monophase composition of the marbles explains similar contour images of the texture and velocity stereoplots (compare the *c*-axis pole figure and texture-derived velocity distribution of sample TW4 in Figs. 5 and 7 as an example). Comparable contour images can be observed also for the amphibolite sample TW11 containing hornblende as the only texturized component (refer to Figs. 5 and 7 for particular stereoplots). The degree of P-wave anisotropy ($A=4.4\%$) is considerably higher as for the gneisses but smaller as for the marbles (Fig. 8). The mean velocities of marbles and amphibolite are com-

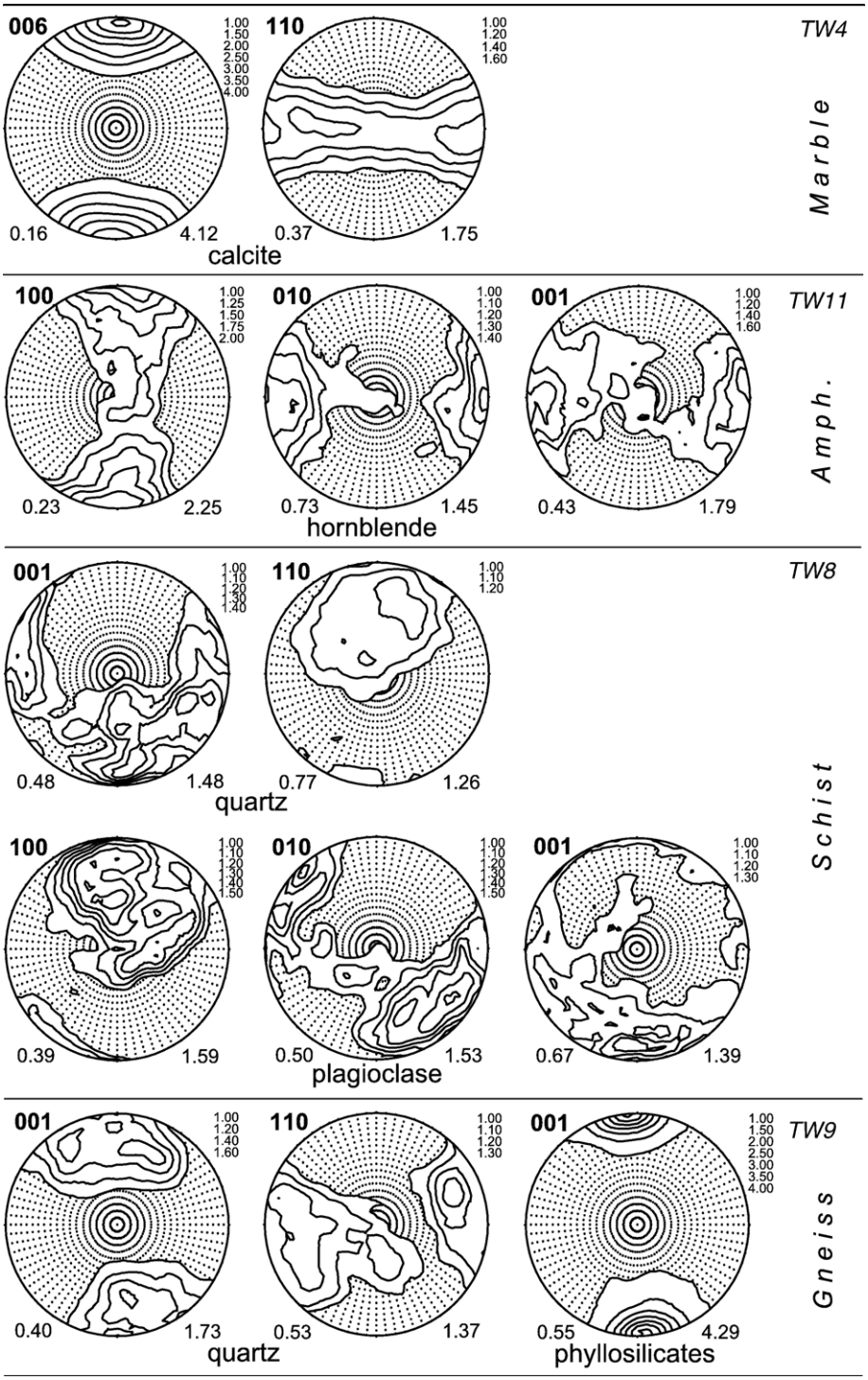

Fig. 5. Recalculated pole figures of some samples, selected according to their importance for the interpretation of P-wave velocity distributions. Minimum and maximum pole densities are given at the bottom of the stereoplots, dots indicate pole densities less than one time random. The pole figures are shown in sections normal to the macroscopic foliation and parallel to the lineation. *Amph.*: amphibolite.

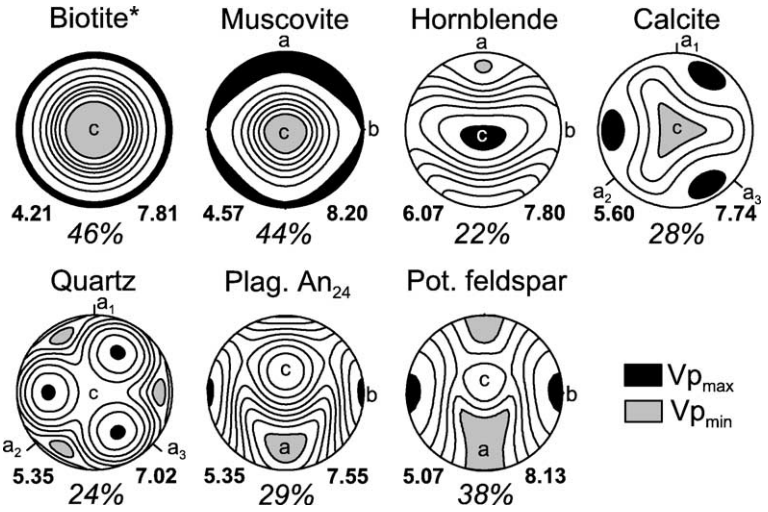

Fig. 6. P-wave velocity distributions and anisotropies of particular minerals. The minimum and maximum velocities are indicated, anisotropies are given in percent (quartz: McSkimin et al., 1965; plagioclase and potassic feldspar: Aleksandrov et al., 1974; muscovite: Vaughan and Guggenheim, 1986; biotite and hornblende: Aleksandrov and Ryzhova, 1961; calcite: Dandekar, 1968). *Considered as hexagonal.

parable (6.82~6.87 km s^{-1}), whereas the mean velocities of the gneisses and slates are generally lower (6.28~6.55 km s^{-1}).

4.2. Experimental P-wave velocity distributions and pore space anisotropies

In addition to the textural influence, experimental estimates of V_p are affected by the crack fabric, leading to somewhat lower velocities compared to the texture-derived velocities. At first sight, the assumption that most cracks are closed at P_{conf}=200 MPa is supported by the crack-induced velocity decrease ΔV_P (the exponential term of Eq. (1)), ranging from 0.000 to 0.030 km s^{-1} (Table 2). Particular experimental velocity distributions at P_{conf}=200 MPa should be, therefore, dominated by the mineral textures. In contrast to these expectations, the mean velocities are lowered by about 0.21~0.51 km s^{-1} (Fig. 7), which is mostly beyond the expected error level of $\pm$0.3 km s^{-1} and therefore considered to be significant (refer to discussion later on). The decrease of the mean velocities is smaller for the marble (TW2, TW4) and amphibolite (TW11) samples compared to the gneisses and schists. Anisotropy A_{200} increases, ranging from 4.4% to 17.5% (Fig. 8). The directions of minimum and maximum velocity of particular velocity distributions perfectly parallel each other for samples TW2, TW4 (marbles) and TW11 (amphibolite), whereas large deviations can be observed for several gneiss samples, e.g., TW3 and TW17 (Fig. 7).

Although complete saturation of the samples with water cannot be ensured, velocity measurements on immersed samples may indicate velocity trends caused by the presence of 'very low velocity' volume parts, like air and water. Compared to the velocity distributions measured at P_{conf}=200 MPa, the immersed samples show a general decrease of the mean velocities by 0.31~1.09 km s^{-1}. The anisotropy parameter of the immersed samples, A_{sat}, is larger compared to its corresponding value A_{200}, except for sample TW1, which displays similar values (Fig. 8). In the extreme case, A_{sat} is about two times A_{200} (sample TW8). The positions of minima and maxima in the stereoplots are slightly different, the largest deviation being observed for sample TW1 (Fig. 7). We failed to measure velocity differences of the marble samples TW2 and TW4, dry and immersed samples displayed the same velocities within the expected error range. This failure is probably due to missing connectivity of pore space owing to the very low porosity. Technical errors occurred at sample TW12. Corresponding data of samples TW2, TW4 and TW12 are therefore missing in Figs. 7–10.

Judging anisotropy coefficients A (α,β), the often high anisotropy of pore space distribution, ranging from 37% to 149% becomes obvious (Fig. 9). No correlation with parameters like e.g. the pore volume could be found, however, in most cases, A_{max} (α,β) subparallels the foliation normal, with the exception of sample TW16. Sample TW16 displays irregular folds in the cm scale, i.e., the foliation plane orientation varies at sample scale. The presence of folds may explain the

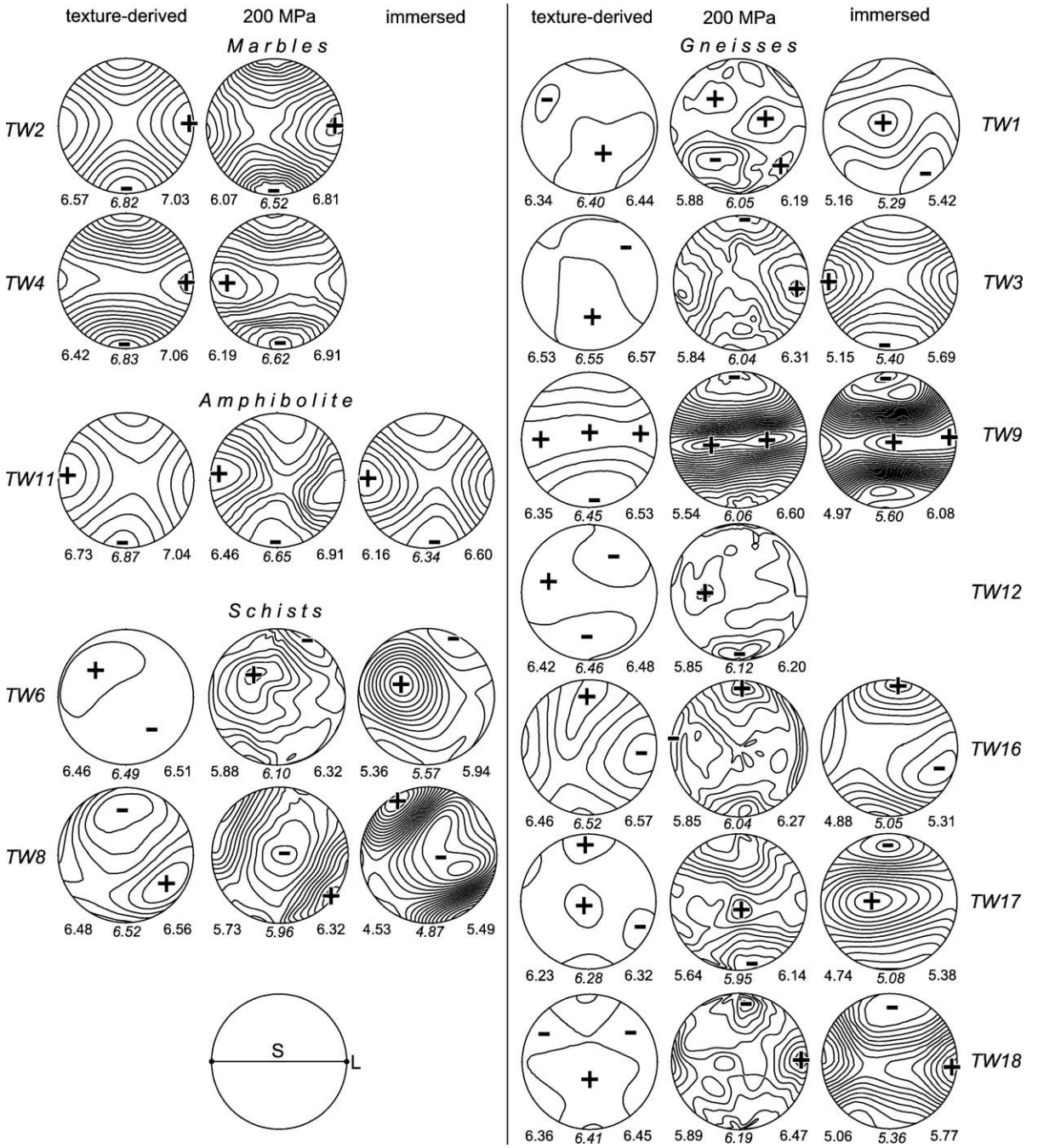

Fig. 7. Calculated ('texture-derived') and experimental ('200 MPa', 'immersed') P-wave velocity distributions. Plots of the immersed samples TW2, TW4 and TW12 were omitted (see text for explanation). Minimum, mean and maximum velocities are given at the bottom of the plots, contour line step size is 0.05 km s^{-1} for all plots. The plus sign indicates regions of high velocity, the negative sign refers to the minimum velocity. The velocity distributions are shown in sections normal to the macroscopic foliation and parallel to the lineation (see sketch at the bottom left).

observed misorientation between the macroscopic foliation plane and the direction of maximum velocity in the difference patterns, and missing preferred orientation of the phyllosilicate basal planes as well (refer to Section 4.1.).

5. Discussion

In addition to an accurate texture determination, which was optimized by application of high resolution neutron diffraction and large sample volumes, the reli-

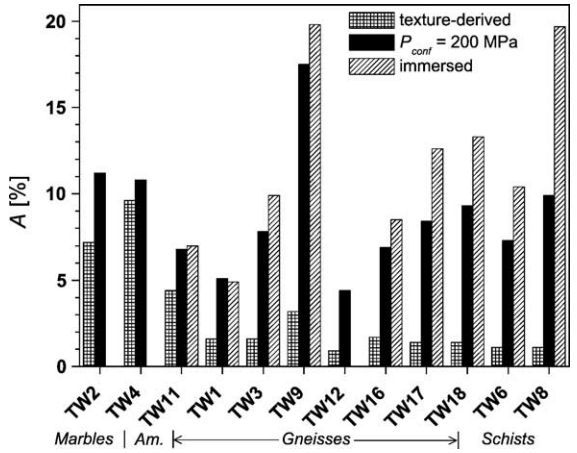

Fig. 8. Comparison of anisotropy parameters $A=(V_{P_{max}}-V_{P_{min}})/V_{P_{mean}}$. Values of the immersed samples TW2, TW4 and TW12 were omitted (see text for discussion). *Am.*: amphibolite.

ability of texture-derived P-wave velocity distributions depends on the exact estimation of rock composition and applied elastic constants of particular minerals. Modal composition of the samples was determined by means of the Rietveld refinement method on X-ray powder diffraction data to minimize errors (see Section 3), whereas the elastic constants had to be taken from the literature. The elastic constants depend on chemical composition, hence, the bulk error level may increase due to chemical variation of particular minerals. Judgement of limiting values indicates that the error of the modelled (texture-derived) velocity distributions is about ± 0.1 km s^{-1}, empirical estimates suggest the same level for the experimental P-wave data. Moreover, application of different equipment may cause methodical errors. Comparing velocity data gained on dry samples at atmospheric pressure (using equipment at IFP) with velocity data obtained at comparable pressure level $P_{conf}=2$ MPa (using equipment at GZG) indicates systematically higher velocities in the order of 100~200 m s^{-1} for the IFP equipment. Consequences are due to the similarity of data gained at $P_{conf}=200$ MPa (GZG) and data from the immersed samples (IFP). We have no criterion to find out the 'true' velocity level. However,

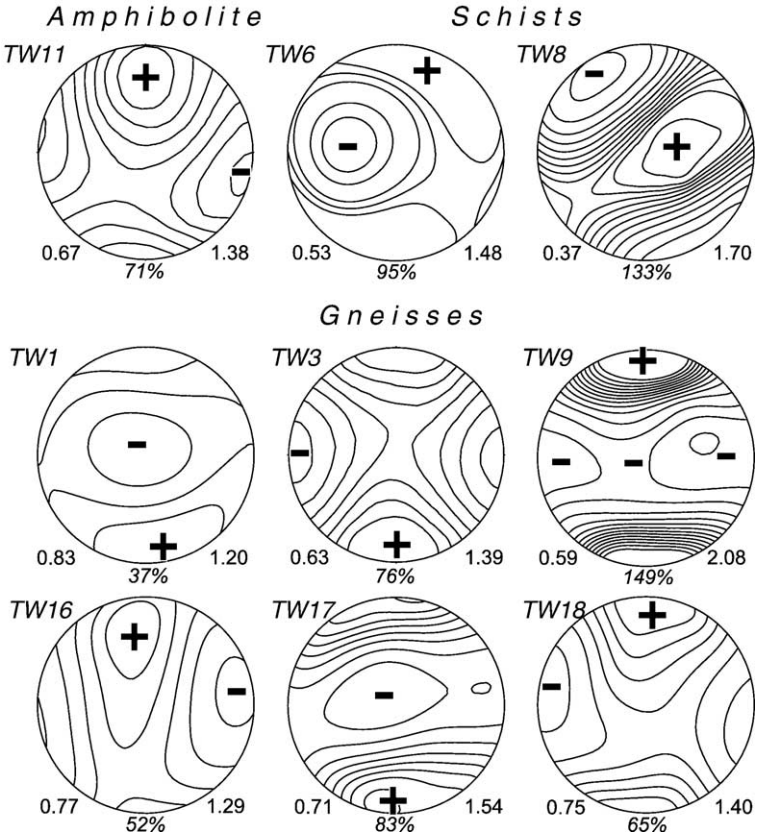

Fig. 9. Anisotropy coefficients $A(\alpha,\beta)$ to illustrate pore space distributions, shown in sections normal to the macroscopic foliation and parallel to the lineation. Extreme values and anisotropies (in percent) of particular distributions are given at the bottom of the plots, plus and minus signs refer to the maximum and minimum, respectively.

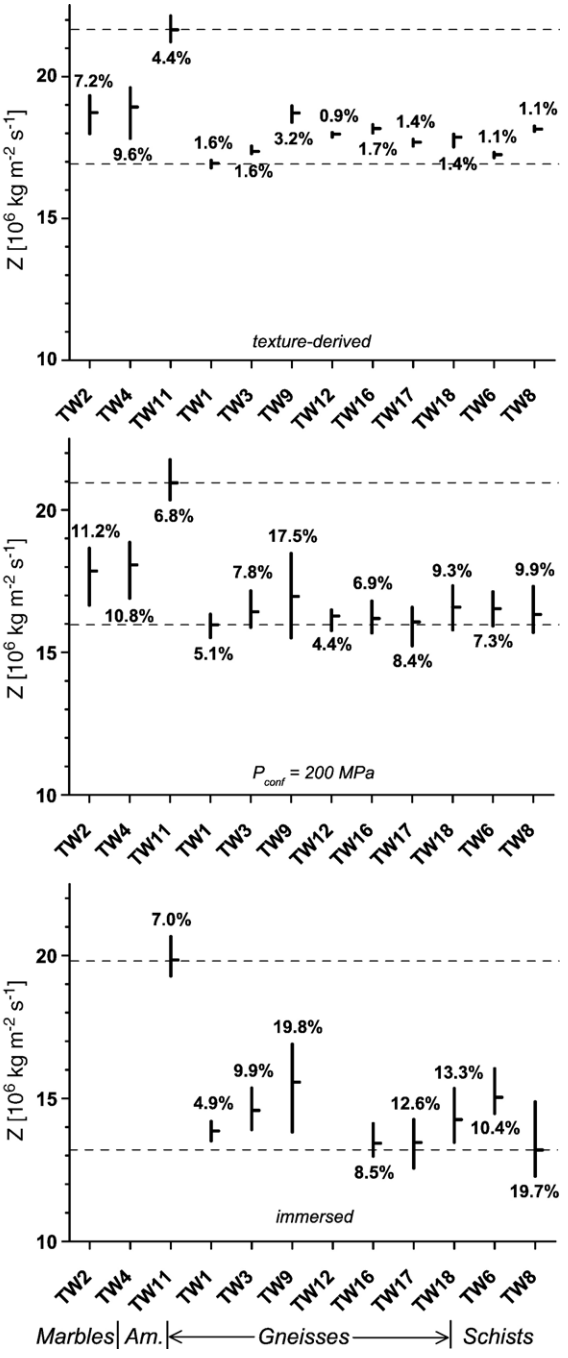

Fig. 10. Acoustic impedances $Z=\rho V_p$ of 'texture-derived' and experimental ('P_{conf}=200 MPa', 'immersed') velocity distributions. The range of acoustic impedances is indicated by a vertical bar, the mean value by a tick mark, anisotropies are given in percent. Horizontal dotted lines indicate the scattering of mean values. *Am.*: amphibolite.

for relative comparison of particular data sets the following considerations apply: immersed samples were measured at atmospheric pressure. Applying gradients dV_p/dP (Table 2), which are assumed to describe mainly the effect of lattice compression, the 'intrinsic' contributions to the velocity magnitudes measured on the immersed samples may be corrected for confining pressure. Remaining velocity differences are consequently caused by the crack fabric. Calculated velocity increase for P_{conf}=200 MPa includes the range 110~300 m s^{-1} and counteracts methodical errors denoted above. Since the magnitude of both these correction terms is approximately the same, velocity distributions measured on the immersed samples are representative for confining pressure P_{conf}=200 MPa, i.e., particular velocity distributions may be compared directly as they are. Assuming that methodical errors also are of magnitude ±0.1 km s^{-1}, the maximum bulk error approaches ±0.3 km s^{-1}.

5.1. Calculated velocity distributions versus velocity distributions at P_{conf}= 200 MPa

The difference between texture-derived and experimental P-wave velocities is generally interpreted in terms of open cracks. Since the crack-induced velocity decrease $\Delta V_p = -c_p 10^{-P_{conf}/d_p}$ approximates zero for P_{conf}=200 MPa (see Table 2 for values), most cracks are expected to be closed and the velocities calculated from Eq. (1) should match the texture-derived velocities. However, velocity differences up to 0.51 km s^{-1} are observed (experimental velocities are consistently lower), which are clearly beyond the expected error level. The question arises, whether decomposition of the pressure–velocity equation into its 'intrinsic' and 'extrinsic' components according to Eq. (1) is reliable. The small number of data for the fit (especially for the pressure interval 200~400 MPa) and restriction to a maximum confining pressure of 400 MPa (which may be too low for precise description of the linear term of Eq. (1)) imply that large errors must be assigned to the velocity difference ΔV_P. For that reason, magnitudes of ΔV_P are not interpreted, however, the conclusion seems to be justified that the 'extrinsic' (crack-related) contribution to V_P at P_{conf}=200 MPa is actually small. With regard to subsequent discussion of P-wave anisotropy, we also want to emphasize that calculation of the anisotropy parameter A is not falsified by erroneous magnitudes of V_P, provided that deviations of V_P from the 'true' value are consistent to lower (or higher) velocities and small compared to the magnitude of V_P.

Comparing texture-derived and experimental P-wave anisotropies obtained at P_{conf}=200 MPa, the minor role of the mineral textures for many samples becomes obvious. This observation finds its visual expression in dissimilar contour line patterns and dis-

similar positions of the minimum and maximum velocities (Fig. 7) and in rather low anisotropy parameters A_{tex} of magnitude 1% to 2% (Fig. 8). The crack fabric clearly determines the experimental velocity distribution in the case of weak textures, as indicated by much higher anisotropies A_{200} and crack-related anisotropy contributions A_{200}–A_{tex} (the range of A_{200}–A_{tex} for these samples is 3.5~14.3). The mean values of acoustic impedances $Z_{mean} = \rho V_{p_{mean}}$ are in fact identical, ranging between 16 and 22 [10^6 kg m^{-2} s^{-1}] (Fig. 10). Hence, any calculation based on mean values can be performed either on texture-derived or experimental velocity data leading to similar results.

Predominance of well-pronounced textures (samples TW2, TW4, TW11) may be inferred from similar contour line patterns and similar orientations of the minimum and maximum velocities in particular pole figures and velocity distributions. Concerning calcite (samples TW2, TW4), the direction of minimum velocity coincides with the direction of maximum pole density of the *c*-axis pole figure (Figs. 5 and 7). Both these principal directions are subparallel to the foliation normal, in agreement with commonly observed natural textures (e.g., Wenk et al., 1987). In case of hornblende (sample TW11), the minimum velocity coincides with the (100) pole figure maximum and the maximum velocity with the (001) pole figure maximum (Figs. 5 and 7). In conformity with most natural textures (e.g., Siegesmund et al., 1994; Ivankina et al., 1999), the (100) intensity maximum parallels the foliation pole. Consequently, the minimum velocity parallels the foliation pole as well. Anisotropy A_{200} of the amphibolite (6.8%) approximates the value given by Mazzoli et al. (2002) for P_{conf}=200 MPa ($\approx$ 8%), however, differences are due to the symmetry of particular velocity distributions. Our P-wave measurements indicate orthorhombic symmetry (this holds true for the texture-derived velocity distribution as well), whereas the measurements of Mazzoli et al. (2002) in three mutually perpendicular directions show transverse isotropic symmetry. This observation may be due to a possible coincidence of the measured directions and the directions of minimum and maximum velocity. The symmetry of P-wave measurements on amphibolites from the Kola peninsula is generally orthorhombic (Kern et al., 2001), which, therefore, appears to be the most common symmetry state of deformed amphibolites.

Taking into account the pore space distribution with its maximum dimension close to the foliation pole, it may be inferred that fluids lead to some reduction of bulk rock anisotropy, although the textural influence predominates (but refer to discussion in Section 5.2.). Increasing importance of the textures finds its expression also in the crack-related part A_{200}–A_{tex} of bulk rock anisotropy (ranging from 1.2% to 4.0%), which is much smaller than the texture-related contribution A_{tex} (4.4~9.6%).

The well-developed transverse isotropic phyllosilicate texture of sample TW9 has large influence on P-wave anisotropy (compare particular plots in Figs. 5 and 7), although the extremely anisotropic pore space distribution (A=149%; Fig. 9) lets us assume considerable influence of the crack fabric. In contrast to our observations, experimental velocity distributions of phyllonites/phyllites reported by Mazzoli et al. (2002) show orthorhombic symmetry, which is attributed to crenulation of the phyllosilicate basal planes with the mineral lineation as the crenulation axis. Missing crenulation in sample TW9 explains transverse isotropic symmetry of texture-derived and experimental velocity distributions. Anisotropies are comparable to our data (19~24%; A_{200} of sample TW9: 17.5%), however, maximum velocities are significantly higher ($\approx$ 7 km s^{-1}; sample TW9: 6.6 km s^{-1}). Very large amounts of phyllosilicates (65~81%) with $V_{p_{max}}$ 8 km s^{-1} perpendicular to the basal plane (compare to Fig. 6) may account for the observed velocity difference. Increasing importance of the crack fabric finds its expression also in much higher crack-related anisotropy compared to the texture derived anisotropy (A_{200}–A_{tex}=14.3%, A_{tex}=3.2%), but refer to the following section for discussion of these quantities.

5.2. Effect of fluids/porosity

The effect of fluid-filled intergranular pore space on the acoustic properties of low-porosity rocks may be twofold. First, P-wave velocity (and consequently acoustic impedance Z as well) decreases, second, anisotropy may change, since all the pore space distributions are anisotropic. At first sight, the measurements on immersed samples indicate a general shift of acoustic impedances Z to smaller values, as illustrated by the range of mean impedances Z_{mean} (13.2~19.8 [10^6 kg m^{-2} s^{-1}]; Fig. 10). This holds true for all samples, anisotropies up to 19.8% are observed. However, the extent of velocity reduction conflicts with theoretically calculated values.

It is beyond the scope of the paper to discuss whether crustal fluids are in fact present or not, however, we intend to discuss its potential influence on the basis of the pore space geometry detected at surface conditions. The hypothesis is that pore space distribution caused by decompression during exhumation resembles pore space distribution caused by hydraulic fracturing in the depth. This is supported by the observation that

the maximum anisotropy coefficient A_{max} (α,β) is related to the predominant foliation plane, which is known to represent the most prominent mechanical anisotropy plane formed during ductile deformation processes at great depth (e.g., Oertel, 1983).

Several attempts were made to quantify the effect of dry and fluid-filled pore space on the elastic wave propagation velocities. Theoretical models (e.g., O'Connell and Budiansky, 1974; Kachanov, 1992) try to calculate crack-induced changes of the elastic moduli from differences in the energy state of the uncracked and cracked solid. Interdependencies are complicated, the main controlling factors are the frequency (over-all volume fraction), shape (aperture to diameter aspect ratio), arrangement (distribution and preferred orientation of cracks with large aspect ratio), size (many small cracks are less effective than few large cracks with the same total volume) and interaction of cracks, as well as the occurrence of fluids. For low-porosity rocks, the model calculations of O'Connell and Budiansky (1974) are in good agreement with experimental data (Popp and Kern, 1994) Dependence of the elastic moduli on effective pressure P_{eff} has been observed in experimental studies (e.g., Reuschlé et al., 2003). Effective pressure not necessarily equals confining pressure P_{conf}, but may be reduced by apparent pore pressure P_{pore} according to $P_{eff}=P_{conf}-\eta P_{pore}$, where the coefficient η is smaller than unity and depends on P_{conf} as well (Todd and Simmons, 1972).

In order to quantify the volumetric effect of fluid-filled pore space on P-wave propagation velocity at constant confining pressure of $P_{conf}=200$ MPa, particular velocity distributions were taken as base line values for addition of various amounts of pore space X (1%, 2%, 3% and 5%), with pore space geometry characterized by coefficients A (α,β) as given in Fig. 7. This may not be a precise simulation of pore space distribution at depth, since small fractions of open cracks may be present even at $P_{conf}=200$ MPa. However, the crack-related velocity difference ΔV_P (ranging from 0.000 to -0.030 km s^{-1}; Table 2) indicates that the initial pore volume is rather small at 200 MPa, and thus the pore volume added to the samples approximates the total pore volume. Including the P-wave velocity in water (1.53 km s^{-1}), the modeled velocity V_p (α,β) was calculated for any sample direction (α,β) according to

$$V_p(\alpha,\beta) = w\ 1.53\ A(\alpha,\beta) + (1-w)V_{P_{200Mpa}}(\alpha,\beta), \quad (3)$$

where $w=X/100$, the volume fraction weight coefficient.

As expected, P-wave velocitiy decreases with increasing simulated pore volume X (in Fig. 11, trends of $V_{P_{min}}$, $V_{P_{max}}$ and $V_{P_{mean}}$ are given). Gradients $dV_{P_{mean}}/dX$ include the range -0.044 to -0.066 [km s^{-1} vol.%$^{-1}$], its reciprocal values (the amount of pore space, at which $V_{P_{mean}}$ is reduced by 1 km s^{-1}) range from 15.2 to 22.7 [vol.% km^{-1} s] (Fig. 11). This means that rather large amounts of pore space are required for considerable velocity decrease following our model. In a few cases, anisotropy changes may be inferred from converging trends of $V_{P_{min}}$ and $V_{P_{max}}$. Sample TW1 displays a weak reduction of anisotropy, whereas anisotropy of samples TW6 and TW8 decreases by approx. 1% (Fig. 12). All the other samples are invariant with respect to anisotropy modification. As a conclusion, we show that the volumetric effect of pore volume changes of a few percent seems to be too small to change V_P anisotropy significantly.

Velocities calculated in such a way differ significantly from the velocities measured on the immersed samples, as indicated for $V_{P_{min}}$, $V_{P_{max}}$ and $V_{P_{mean}}$ in Fig. 11. They are consistently higher, differences include the range 0.2~1.1 km s^{-1} with the smallest deviation due to the amphibolite (sample TW9). Such large discrepancies are obviously beyond the expected error range of ± 0.3 km s^{-1}. Ion exchange (replacement of the interlayer cation K^+ by the hydronium cation H_3O^+ in muscovite) is non-expansive (McGuiggan and Israelachvili, 1990; Cheng et al., 2001). Thus, no effect on the elastic wave propagation velocities due to lattice widening of the phyllosilicates is expected. Alternatively, uncompleted saturation of pore space with water, with air remaining in part of the pore space, may explain observed velocity difference. However, the amount of air-filled pore space, which is required to bring the experimental data into agreement with the modeled data, is high (2~16%, considering $V_{P_{mean}}$) and, therefore, implausible to explain most of observed velocity decrease. Assuming, for instance, that only 50% of the real pore volume are filled with water, the effect of still air-filled pore space on $V_{P_{mean}}$ is -0.07 to -0.36 km s^{-1}. Values close to the lower boundary of the interval (corresponding to small pore volumes) are more realistic, because connectivity of cracks improves with increasing bulk pore volume and degree of saturation moves towards 100%. Thus, required correction for uncompleted saturation is assumed to be 0.1~0.2 km s^{-1}, or less.

Concluding, remaining discrepancies between modeled velocities and velocities measured on the immersed samples must be interpreted in terms of direct crack effects like, e.g., crack aspect ratio, crack pre-

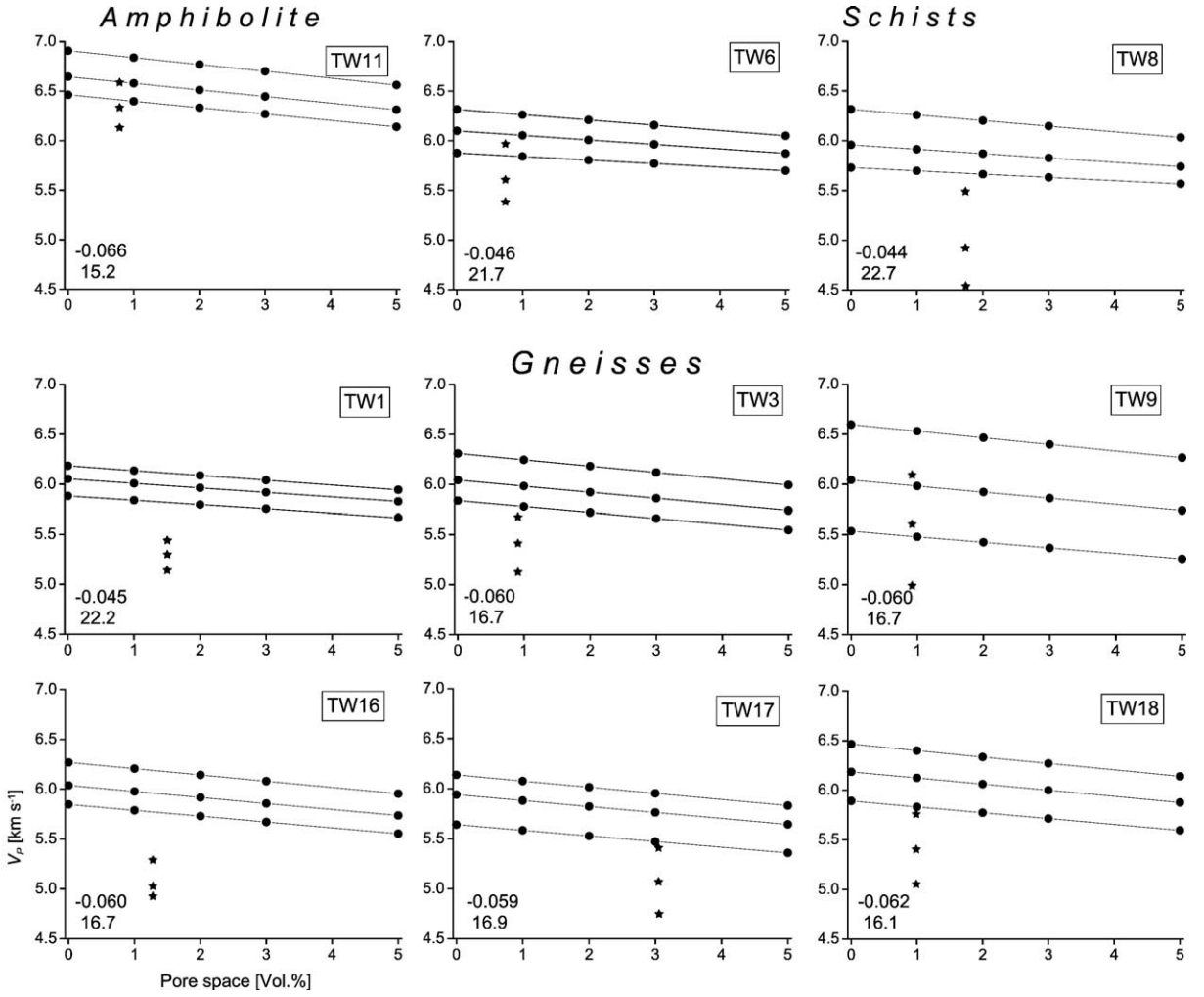

Fig. 11. Decrease of principal velocities $V_{P_{min}}$, $V_{P_{max}}$ and $V_{P_{mean}}$ at P_{conf}=200 MPa in dependence on the amount of water-filled pore space, added to the velocity distribution measured at P_{conf}=200 MPa. Numbers within the diagrams indicate gradients $dV_{P_{mean}}/dX$ (top; X: pore space), and the pore volume X_1 leading to velocity decrease of 1 km s^{-1} (bottom). Principal values measured on the immersed samples are indicated by stars.

ferred orientation and crack interaction. These parameters are not directly accessible in an experiment but may be successfully modeled. In spite of pronounced pore space anisotropy (Fig. 9), the volumetric effect of water-filled pore space on P-wave anisotropy is small (Figs. 11 and 12).

In view of the fact that hydraulic fracturing of rocks by means of migrating fluids requires pore pressures close to confining pressure (e.g., Etheridge, 1983), the influence of pore pressures on P-wave velocities should be included into discussion. Experimental estimates of pore pressure effects on granite samples indicate P-wave velocity decrease of $\Delta V_P = -0.077$ km s^{-1} (Todd and Simmons, 1972; constraints: P_{conf}=200

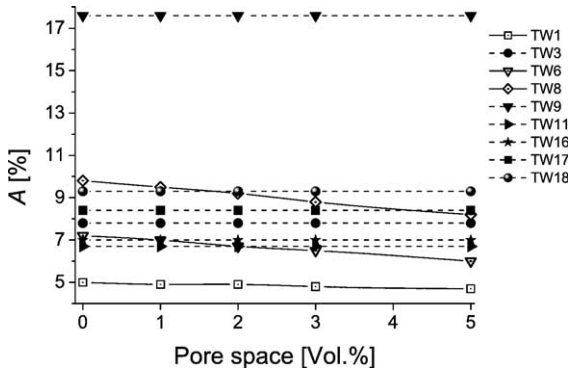

Fig. 12. Variation of anisotropy A in dependence on the amount of water-filled pore space X. For explanations refer to Fig. 9.

MPa, P_{pore}=105 MPa, porosity: 0.5%) and ΔV_P=−0.15 km s^{-1} (Reuschlé et al., 2003; P_{conf}=75 MPa, P_{pore}=70 MPa, porosity: 1.2%). Applying these magnitudes to our samples, which appears to be justified due to comparable porosities (Table 2), we expect pore pressure effects of magnitude −0.1 to −0.2 km s^{-1} at confining pressure of 200 MPa.

5.3. Reflectivity of lithological interfaces

Seismic reflections are caused by contrasts in acoustic impedances $Z=\rho V_p$ of neighbouring units in the deep Earth. Neglecting velocity anisotropy and assuming that the units are thick enough to produce a detectable signal and the incoming beam is normal to the interface, let us calculate the reflectivity of a lithological interface according to

$$R_c = \frac{\bar{Z}_1 - \bar{Z}_2}{\bar{Z}_1 + \bar{Z}_2}, \quad (4)$$

where R_c is the reflection coefficient, and Z is the weighted mean of 100 sample directions. Such a simplified reflection coefficient, which considers mean values only, may be sufficient for semi-quantitative estimations. The maximum possible reflection coefficient calculated from texture-derived acoustic impedances according to these constraints would be $R_{c_{max}}$=0.12, corresponding to a gneiss (TW1)–amphibolite (TW11) contact. Approximately the same value ($R_{c_{max}}$=0.13) is obtained for the same lithological contact from measurements at confining pressure P_{conf}=200 MPa. This is sufficient to produce a strong reflection (Warner, 1990), and is principally caused by the density contrast between both units (refer to Table 2). For a gneiss–marble contact (e.g., TW1—gneiss and TW4—marble) the maximum reflection coefficient is about $R_{c_{max}}$=0.06. This holds true for experimental and texture-derived data. Even such a signal amplitude should produce a clear signal (Jones and Nur, 1982).

Up to this point, discussion is based on the maximal possible reflection coefficients to be expected from our data for the rock contacts in the TRANSALP traverse. Contact zones between various types of gneisses (consider samples TW12, TW16, TW17, TW18) lead to reflection coefficients of $R_c \leq 0.02$. Reflections at such lithological contacts are expected to produce an exploitable signal only at optimal experimental conditions in a reflection seismic experiment.

Possible effects of fluids on seismic reflectivity may be assessed by considering juxtaposition of one and the same sample at ‘wet’ and ‘dry’ conditions. Using mean values from our study, reflection coefficients calculated in such a way range from 0.026 to 0.104, where $V_{P_{mean}}$ of the ‘dry’ samples was derived from the velocity distributions obtained at P_{conf}=200 MPa, and the ‘wet’ samples were considered to contain the amount of water-filled pore space reported in Table 2. In addition, pore pressure induced velocity decrease of −0.15 km s^{-1} was taken into account (refer to discussion in Section 5.2). Magnitudes of R_c indicate that differences in the degree of fluid saturation may affect reflectivity of lithological interfaces significantly, although the extreme case (combination of completely dry and completely saturated series) may be scarce.

6. Conclusions

Our results indicate that principal rocks from the TRANSALP reflection seismic traverse in the Eastern Alps display different degrees of P-wave velocity anisotropy on the laboratory scale. The texture-derived contribution to anisotropy of most gneisses and schists is small due to weak or missing crystallographic preferred orientations, even of the phyllosilicates. Microfolding of the rock foliation on sample scale explains our observations. As a consequence, P-wave anisotropy in most schists and gneisses appears to be dominated by the crack fabric. We suspect that this is a common feature of (micro)folded gneisses and schists, which may be quickly checked by analyzing the basal plane crystallographic preferred orientations of the phyllosilicates.

Only the ‘monophase’ samples (marbles and amphibolites) and a single gneiss sample display distinct P-wave anisotropy due to well-pronounced mineral textures, leading to predominance of the texture-related portion of bulk rock anisotropy.

Pore space distributions at surface conditions are extremely anisotropic with the maximum dimension mostly parallel to the foliation normal. Principal directions of the texture-related and crack-related anisotropy contributions are subparallel to each other and subtractive, i.e., the effect of pore space on anisotropy compensates the effect of the mineral textures to some extent.

Numerical calculation of the volumetric effect of water-filled pore space at confining pressure P_{conf}=200 MPa indicates that a few volume percent of water-filled cracks have an effect on P-wave velocity gradients on the order of −50 m s^{-1} vol.%$^{-1}$. Anisotropy effects are not influenced generally. Experimental velocity estimates on immersed samples, corrected for confining pressure P_{conf}=200 MPa, display much lower velocities (up to −1.1 km s^{-1} for the actual

pore volume) and an increase of anisotropy by a few percent. Direct crack effects seem to be the most reliable explanation, although incomplete saturation of pore space with water may explain part of the effect.

Judging reflection coefficients calculated from our experimental data, one general conclusion with respect to the TRANSALP reflection seismic experiments is that strong reflectors are most likely due to pronounced lithological contrasts, such as marble–gneiss or amphibolite–gneiss boundaries. Contacts between various gneisses are unlikely to produce strong reflections, whereas contacts between 'wet' and 'dry' series may lead to clear reflections in dependence on the degree of saturation with fluids.

Acknowledgements

We are grateful to R. Naumann (Potsdam) for quantitative phase analyses. Thorough reviews by L. Burlini (Zürich) and T. Popp (Leipzig) helped to improve the manuscript significantly. Neutron texture measurements were supported by the Frank Laboratory of Neutron Physics, Dubna, Russia. KU and JHB are grateful for financial support through BMBF grant 03-DU0-FRE.

References

Aleksandrov, K.S., Ryzhova, T.V., 1961. The elastic properties of rock forming minerals. Izv. Acad. Sci. USSR, Geophys. Ser. 12, 1799–1804.

Aleksandrov, K.S., Alchikov, U.V., Belikov, B.P., Zaslavski, B.I., Krupnyi, A.I., 1974. Elastic wave velocities in minerals at atmospheric pressure and increasing precision of elastic constants by means of EVM. Izv. Acad. Sci. USSR, Geol. Ser. 10, 15–24.

Arts, R.J., Rasolofosaon, P.N.J., Zinszner, B., 1996. Experimental and theoretical tools for characterizing anisotropy due to mechanical defects in rocks under varying pore and confining pressures. In: Fjaer, E., Holt, R.M., Rathore, J.S. (Eds.), Seismic anisotropy, Soc. Explor. Geophys., Tulsa, pp. 384–432.

Barruol, G., Mainprice, D., Kern, H., de Saint Blanquat, M., Compte, P., 1992. 3D seismic study of a ductile shear zone from laboratory and petrofabric data (Saint Barthélémy Massif, Northern Pyrénées, France). Terra Nova 4, 63–76.

Behrmann, J.H., 1990. Zur Kinematik der Kontinentkollision in den Ostalpen. Geotekton. Forsch 76, 1–180.

Behrmann, J.H., Frisch, W., 1990. Sinistral ductile shearing associated with metamorphic decompression in the Tauern Window. Eastern Alps. Jb. Geol. B.-A. 133, 135–146.

Bergmann, J., Friedel, P., Kleeberg, R., 1998. BGMN—a new fundamental parameters based Rietveld program for laboratory X-ray sources, it's use in quantitative analysis and structure investigations. CDP Newsl. 20, 5–8.

Birch, F., 1960. The velocity of compressional waves in rocks to 10 kilobars: Part I. J. Geophys. Res. 65, 1083–1102.

Bunge, H.-J., 1982. Texture Analysis in Materials Science—Mathematical Methods. Butterworths, London. 593 pp.

Cheng, L., Fenter, P., Nagy, K.L., M.L. Schlegel, M.L., Sturchio, N.C., 2001. Molecular-scale density oscillations in water adjacent to a mica surface. Phys. Rev. Lett. 87, 156103-1–156103-4.

Christensen, N.I., 1965. Compressional wave velocities in metamorphic rocks at pressures to 10 kilobars. J. Geophys. Res. 70, 6147–6164.

Dandekar, D.P., 1968. Variation in the elastic constants of calcite with pressure. AGU Trans. 49. 323 pp.

Etheridge, M.A., 1983. Differential stress magnitudes during regional deformation and metamorphism: upper bound imposed by tensile fracturing. Geology 11, 231–234.

Godfrey, N.J., Christensen, N.I., Okaya, D.A., 2000. Anisotropy of schists: contribution of crustal anisotropy to active source seismic experiments and shear wave splitting observations. J. Geophys. Res. 105, 27991–28007.

Ivankina, T.I., Nikitin, A.N., Lokajicek, T., Pros, Z., Klima, K., Ullemeyer, K., 1999. Textures and elastic anisotropies of amphibolites from the Kola borehole. NRC Res. Press 1999, 1587–1592.

Jones, T., Nur, A., 1982. Seismic velocity and anisotropy in mylonites and the reflectivity of deep crustal fault zones. Geology 10, 260–263.

Kachanov, M., 1992. Effective elastic properties of cracked solids: critical review of some basic concepts. Appl. Mech. Rev. 45, 304–335.

Kern, H., 1993. P- and S-wave anisotropy and shear wave splitting at pressure and temperature in possible mantle rocks and their relation to the rock fabric. In: Mainprice, D., Vauchez, A., Montagner, J.-P. (Eds.), Dynamics of the Subcontinental Mantle: From Seismic Anisotropy to Mountain Building, Phys. Earth Planet. Int., vol. 78, pp. 245–256.

Kern, H., Popp, T., Gorbatsevich, F., Zharikov, A., Lobanov, K.V., Smirnov, Yu.P., 2001. Pressure and temperature dependence of V_P and V_S in rocks from the superdeep well and from surface analogues at Kola and the nature of velocity anisotropy. Tectonophysics 338, 113–134.

Kern, H., Jin, Z., Gao, S., Popp, T., Xu, Z., 2002. Physical properties of ultrahigh-pressure metamorphic rocks from the Sulu terrain, eastern central China: implications for the seismic structure at the Donghai (CCSD) drilling site. Tectonophysics 354, 315–330.

Kontny, A., Duyster, J., Grawinkel, A., Hoffmann, A., Kamm, C., Machon, L., Rauen, A., Röckel, Th., Spangenberg, E., de Wall, H., Winter, H., 1994. The lithological profile of the KTB Hauptbohrung (7200–8729.7 m). Results from the KTB field laboratory. KTB Rep. 94-2, A1–A13.

Lammerer, B., 1986. Das Autochthon im westlichen Tauernfenster. Jahrb. Geol. B.-A. 129, 51–67.

Lammerer, B., Weger, M., 1998. Footwall uplift in an orogenic wedge: the Tauern Window in the Eastern Alps of Europe. Tectonophysics 285, 213–230.

Lüschen, E., Sobolev, S., Werner, U., Söllner, W., Fuchs, K., Gurevich, B., Hubral, P., 1993. Fluid reservoir (?) beneath the KTB drillbit indicated by seismic shear-wave observations. Geophys. Res. Lett. 20, 923–926.

Lüschen, E., Bram, K., Söllner, W., Sobolev, S., 1996. Nature of seismic reflections and velocities from VSP-experiments and borehole measurements at the KTB deep drilling site in southeast Germany. Tectonophysics 264, 309–326.

Mainprice, D., Barruol, G., Ben Ismail, W., 2000. The seismic anisotropy of the Earth's mantle: from single crystal to polycrystal. Geophys. Monogr. 117, 237–264.

Mancktelow, N.S., Stöckli, D.F., Grollmund, B., Müller, W., Fügenschuh, B., Viola, G., Seward, D., Villa, I.M., 2001. The

DAV and the Periadriatic Fault System in the Eastern Alps south of the Tauern Window. Int. J. Earth Sci. 90, 593–622.
Matthies, S., Vinel, G.W., 1982. On the reproduction of the orientation distribution function of texturized samples from reduced pole figures using the conception of a conditional ghost correction. Phys. Status Solidi (b) 112, K111–K120.
Mazzoli, C., Sassi, R., Burlini, L., 2002. Experimental study of the seismic properties of the Eastern Alps (Italy) along the Aurina-Tures-Badia valleys transect. Tectonophysics 354, 179–194.
McGuiggan, P.M., Israelachvili, J.N., 1990. Adhesion and short-range forces between surfaces: Part II. Effects of surface lattice mismatch. J. Mater. Res. 5, 2232.
McSkimin, H.J., Anreatch, P., Thurston, R.N., 1965. Elastic moduli of quartz versus hydrostatic pressure at 25 and −195.8 °C. J. Appl. Phys. 36, 1624–1632.
Millahn, K., Lüschen, E., Gebrande, H., TRANSALP Working Group, 2005. TRANSALP-cross-line recording during the seismic reflection transect in the Eastern Alps. Tectonophysics, 414, 39–49 doi:10.1016/j.tecto.2005.10.029 (this volume).
Mooney, W.D., Meissner, R., 1992. Multi-genetic origin of crustal reflectivity: a review of seismic reflection profiling of the continental lower crust and Moho. In: Fountain, D.M., Arculus, R., Kay, R.W. (Eds.), Continental Lower Crust. Elsevier, Amsterdam, pp. 45–79.
Nur, A., Simmons, G., 1969. The effect of porosity on velocity in low porosity rocks. Earth Planet. Sci. Lett. 7, 183–193.
O'Connell, R.J., Budiansky, B., 1974. Seismic velocities in dry and saturated cracked solids. J. Geophys. Res. 79, 5412–5426.
Oertel, G., 1983. The relationship of strain and preferred orientation of phyllosilicate grains in rocks—a review. Tectonophysics 100, 413–447.
Platt, J.P., Behrmann, J.H., Cunningham, P.C., Dewey, J.F., Helman, M., Parish, M., Shepley, M.G., Wallis, S., Weston, P.J., 1989. Kinematics of the Alpine arc and the motion history of Adria. Nature 337, 158–161.
Popp, T., Kern, H., 1994. The influence of dry and water saturated cracks on seismic velocities of crustal rocks—a comparison of experimental data with theoretical models. Surv. Geophys. 15.5, 443–465.
Pros, Z., Lokajíček, T., Klíma, K., 1998. Laboratory study of elastic anisotropy on rock samples. Pure Appl. Geophys. 151, 619–629.
Pros, Z., Lokajíček, T., Přikryl, R., Klíma, K., 2003. Direct measurement of 3D elastic anisotropy on rocks from the Ivrea Zone (Southern Alps, NW Italy). Tectonophysics 370, 31–47.
Rabbel, W., Siegesmund, S., Weiss, T., Pohl, M., Bohlen, T., 1998. Shear wave anisotropy of laminated lower crust beneath Urach (SW Germany): a comparison with xenoliths and with exposed lower crustal sections. Tectonophysics 298, 337–356.
Reuschlé, T., Gbaguidi Haore, S., Darot, M., 2003. Microstructural control on the elastic properties of thermally cracked granite. Tectonophysics 370, 95–104.
Siegesmund, S., 1996. The significance of rock fabrics for the geological interpretation of geophysical anisotropies. Geotekton. Forsch. 85, 1–123.
Siegesmund, S., Helming, K., Kruse, K., 1994. Complete texture analysis of a deformed amphibolite: comparison between neutron diffraction and U-stage data. J. Struct. Geol. 16, 131–142.
Todd, T., Simmons, G., 1972. Effect of pore pressure on the velocity of compressional waves in low-porosity rocks. J. Geophys. Res. 77, 3731–3743.
Tomé, C.N., 1998. Tensor properties of textured polycrystals. In: Kocks, U.F., Tomé, C.N., Wenk, H.-R. (Eds.), Texture and Anisotropy. Cambridge University Press, Cambridge, pp. 282–325.
TRANSALP Working group, 2002. First deep seismic reflection images of the Eastern Alps reveal giant crustal wedges and transcrustal ramps. Geophys. Res. Lett. 29 (10), doi:10.1029/2002GL014911.
Ullemeyer, K., Spalthoff, P., Heinitz, J., Isakov, N.N., Nikitin, A.N., Weber, K., 1998. The SKAT texture diffractometer at the pulsed reactor IBR-2 at Dubna: experimental layout and first measurements. Nucl. Instrum. Methods Phys. Res. A412, 80–88.
Vaughan, M.T, Guggenheim, S., 1986. Elasticity of muscovite and its relationship to crystal structure. J. Geophys. Res. 91, 4657–4664.
Warner, M., 1990. Absolute reflection coefficients from deep seismic reflections. Tectonophysics 173, 15–23.
Wenk, H.-R., Takeshita, T., Bechler, E., Erskine, B.G., Matthies, S., 1987. Pure shear and simple shear on calcite textures. Comparison of experimental, theoretical and natural data. J. Struct. Geol. 9, 731–745.
Wenk, H.-R., Matthies, S., Donovan, J., Chateignier, D., 1998. BEARTEX, a Windows-based program system for quantitative texture analysis. J. Appl. Cryst. 31, 262–269.